International Journal of Aeronautical and Space Sciences (2025) 26:562–577
https://doi.org/10.1007/s42405-024-00780-y

IJASS
International Journal of Aeronautical and Space Sciences

ORIGINAL PAPER

# Investigation of a Variable Camber Morphing Airfoil via SMA Wire and Corrugated Structures

**Reem Aly**[1] · **Erdoğan Kaygan**[2] · **Volkan Esat**[1] · **Ali Atashbar Orang**[1]

Received: 23 February 2024 / Revised: 18 June 2024 / Accepted: 25 June 2024 / Published online: 12 July 2024

**Abstract**

This study proposes a novel design concept of SMA wire technology that is applied to an Eppler E397 morphing airfoil. The study suggests replacing a conventional flap like structure which is typically located at 75% chord with a smooth geometry morphing flap positioned at 65% chord. The morphing flap is assumed to be actuated by a shape memory alloy wire and compliant structure mechanism instead of a conventional hydraulic system. The design concept is studied and verified by conducting a finite element analysis to check the structural integrity. A parametric study was then conducted on the number and position of the wire within the airfoil to investigate the amount of downward deflection that can result from the proposed mechanism. As a result, the amount of deflection angle increased directly as the position of the wire approached the upper surface of the airfoil (up to 8.2°). In addition, aerodynamic parameters resulting from the deflected geometries were evaluated using Athena vortex lattice methods (AVL) and then compared to a conventional airfoil with hinged flap-like-structure. The results showcased an increase in lift coefficient, a decrease in drag coefficient, and enhanced aerodynamic efficiency of the morphing flap-like-structure.

**Keywords** Aerodynamic · Corrugated · FEM · Morphing · SMA

## 1 Introduction

In aims of achieving a wide range of flight regimes and to enhance overall performance, researchers have been studying and investigating morphing structures that can easily shapeshift and change their geometries without the disadvantage of having discontinuities or sharp bend angles. Conventional control surfaces such as flaps, slats, or ailerons usually come with disadvantage of having kinks and sharp bend angles [1]. Morphing aircraft structures have the advantage of creating smooth continuous geometry changes while contributing in reducing the overall weight of the wing as well as providing enhanced aerodynamic performance [2–4]. A variable camber within an airfoil can have the ability to enhance aerodynamic efficiency which consequently results in an effective reduction of fuel consumption.

Different types of morphing concepts and design proposals were both studied theoretically and experimented with in several previous studies in aims of achieving improved flight efficiency [5–8]. Morphing structures need to possess the stiffness to bear external loads and enough flexibility to introduce smooth geometry changes, therefore, advanced materials that have impressive characteristics are usually used to cover both constraints. Morphing structures or design concepts are grouped with other supporting mechanisms that can aid in weight reduction and flexibility of the structures. In most cases, linear actuators or compliant mechanisms are integrated within the design. A very common type of linear actuators or smart materials that are used within the morphing field, are shape memory alloys (SMAs).

Shape memory alloys have the advantage of existing in two phases, namely martensite and austenite where they can

---

Communicated by Piergiovanni Marzocca.

✉ Reem Aly
reem.aly@metu.edu.tr

Erdoğan Kaygan
erdogan.kaygan@lentatek.com

Volkan Esat
volkanesat@gmail.com

Ali Atashbar Orang
orang@metu.edu.tr

[1] Department of Mechanical Engineering, Middle East Technical University NCC, Guzelyurt, 99738 Mersin 10, Turkey

[2] Lentatek Aerospace and Aviation Inc, Ankara, Turkey

exhibit impressive mechanical characteristics such as superelasticity or shape memory effect. Additionally, they have the ability to recover large strains up to 8% and can handle large stresses as well [13, 30]. Shape memory alloys are mainly controlled by their four transformation temperatures and depending on which temperature they are loaded and unloaded at the respective behavior is presented [9, 10]. Surely using SMA as an actuating mechanism is promising since it can replace the use of conventional hydraulics and mechanical joints [11]. Using only a wire as the actuating mechanism can greatly affect weight of the structure as mentioned in [12]. Because of their benefits, SMAs have been thoroughly studied and implemented in the aerospace industry as a linear actuator that can be used to morph the airfoil into the desired altered configuration.

For instance, Almedia et al. [13] studied the possibility of designing a morphing rib with a base airfoil of NACA 0012 that can be actuated by a trained NiTi shape memory alloy that can exhibit the two-way-shape memory effect. The study used two different lengths of wires to investigate the amount of deflection the trailing edge can exhibit consequently then studied the aerodynamic performance of the cambered configurations, where the results showed better aerodynamic performance. Ko et al. [14] proposed the use of a SMA spring instead of a wire along with the use of multiple elements grouped together in which it allows relevant movements hence allowing the airfoil to camber. The proposed mechanism showcased impressive aerodynamic enhancements of up to 72% increment in the lift-to-drag ratio compared to the conventional mechanized flap. Moreover, the use of compliant structures, which can provide flexible and elastic deformations, are also concentrated on since it provides the airfoil structure enough stiffness to bear external loads in direction of span and flexibility in chord direction. Corrugated structures have the ability to bear high loads which can be supported by its stiffness and have the ability to smoothly deform in the chord direction, hence is why they are studied and used in some morphing airfoil applications. Woods et al. [15] implemented the concept of using a bio-inspired compliant structure similar to that of a fish (FishBAC). The integrated structure resembled the skeletal structure of a fish and allowed the airfoil to deform its trailing edge smoothly. Experimental testing showcased a significant increase in lift-to-drag ratio compared to the conventional airfoil. Corrugated structures were used both in the trailing edge and leading edge of a cambered morphing airfoil which was designed by Takahashi et al. [16], in which wind tunnel testing proved enhanced aerodynamic performance.

Very few studies have implemented the use of both shape memory alloy along with corrugated structures. Additionally, most studies focus on designing symmetrical airfoil structures. Therefore, in this present study, the conceptual feasibility of a camber morphing airfoil design that intends to use both a shape memory alloy wire grouped with corrugated structures to imitate the deflection of a conventional hinged flap is investigated. The main aim is to shift the location of the conventional hinged flap to a morphing flap that is mechanized by a wire-pulling mechanism while simultaneously being supported by corrugated structures in the trailing edge. The design is implemented on an unsymmetrical base airfoil, where the design is verified by finite element analysis. Additionally, a parametric study is done on the number and positions of wires that can affect the amount of deflection created by the proposed mechanism. After that, the position of the wire that had the most effect on the resulting deflections were then implemented and the resulting deflected configurations with their respective angles were studied by using Vortex Lattice Methods. The study done on the morphing flap using Vortex Lattice Methods aims to evaluate the enhancement of aerodynamic parameters compared to that of a hinged plain flap structure.

The main aim of this study is to investigate morphing camber concepts using SMA and corrugated structure to improve aerodynamic performance of an aircraft. Therefore, the paper will be organized as follows, the proposed design concept along with the numerical model of the designed morphing airfoil as well as preliminary results and the parametric study is described in Sect. 2. The aerodynamic analysis and the methodology used to compare the enhancement in aerodynamic parameters is described in Sect. 3. Finally, in Sect. 4, conclusion and ending remarks are provided.

## 2 Methodology and Numerical Methods

### 2.1 Design Concept

The airfoil model used for this study is Eppler e397 with 1-m chord, which has a maximum thickness ratio of 13.5% and a camber ratio of 5.3%. The Eppler e397 airfoil is typically used for human powered aircrafts (HPAC) as they have high camber and a high maximum lift coefficient [29]. A typical plain flap is usually located at 75% chord position [17] which is used to alter the camber when deflected downwards. Additionally, the rear spar in a typical wing is located at about 65–75% chord [33], therefore, the design implemented the idea of placing the beginning of the morphing section at exactly 65% chord. Although the morphing flap could have been placed at the same exact location as a typical main flap, the earlier shift of the morphing section should allow the structure to have the required seamless bend as well as provide more surface area that can bend downwards when deflected allowing a smooth flow transition.

The 3D model was then created in a Computer Aided Design software (Autodesk Inventor) with the required design constraints. The drawn airfoil had a 1-m chord and

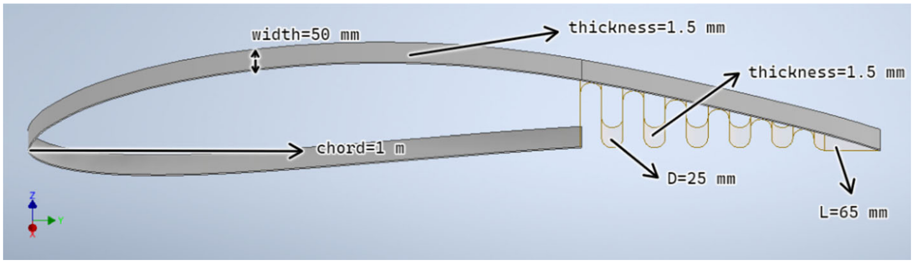

**Fig. 1** Schematic view of the designed morphing airfoil

**Table 1** Geometric dimensions of the morphing airfoil

| Parameters | Dimension |
|---|---|
| Chord | 1000 mm |
| Cross section area | 1.5 mm × 50 mm |
| Radius of corrugated structure | 12.5 mm |
| Diameter of corrugated structure | 25 mm |
| Length of horizontal flat plate (93.5–100%) | 65 mm |
| Number of semi-circular sections | 12 |
| Length of morphing section | 350 mm |
| Thickness of corrugated structures | 1.5 mm |

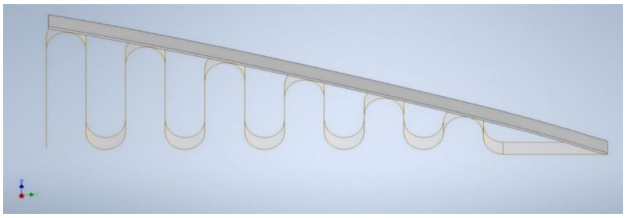

**Fig. 2** Schematic view of the morphing section

a rib-cross section of the whole wing is being considered to test the structural integrity and feasibility of the design in FEA. As indicated in Table 1, the drawn airfoil design has an extrusion length of 50 mm and skin thickness of 1.5 mm as seen in Fig. 1. The morphing section starts from 65% chord till 100% chord; however, the corrugated structures were designed to start at 65% chord till about 93.5% chord then an additional flat plate structure with length of 65 mm was added from 93.5 to 100% chord to increase structural rigidity and prevent the end of airfoil from heavily deforming when it is deflected downwards. The very end of the trailing edge part can be considered as a rigid part, as seen in Fig. 2. The corrugated structures are made of uniform semicircular cross section joined continuously with flat vertical plate sections. The diameter of each semi-circle was set to be 25 mm and the spacing between each 2 consecutive loops is 25 mm. The vertical plates are equally positioned at 25 mm spacing with respect to the diameter of the semi-circular cross sections. Since the enveloped area between the upper and lower surface is getting narrower towards the end of the airfoil, no more vertical plates were added.The variable lengths of the vertical plates connecting the semi-circular loops were based on the enveloping area between the upper surface of the airfoil and lower surface of the airfoil, however in this study the lower part of the airfoil surface in the morphing was not considered in the design and will rather be replaced by a sheet made of flexible skin as [16] suggested in order to facilitate the bending process. The morphing section does not have a hinge axis unlike the conventional plain flap configuration, therefore, the amount of deflection angle that it produces is defined as $\beta$, which is the amount of rotation the morphing section rotates when its deflected downwards.

## 2.2 Morphing Mechanism and Numerical Model

### 2.2.1 Morphing Methodology

The proposed morphing mechanism that is suggested is as follows, the corrugated structures in the trailing edge section in the morphing airfoil model will act as structural support that can help the design bear external loads and perform flexible downward deflection. To actuate the morphing section as shown in Fig. 3, a wire actuating mechanism is inserted. The mechanism will rely on the use of a NiTi shape memory alloy wire since it has the ability to bear large amounts of strain and return back to its pre-strained condition. An assumed actuator as shown in Fig. 3 will be placed in the spar located at 50% where it will be providing the needed pulling action. The pulling mechanism alongside the addition of corrugated structures will manage to generate a flap-like downward deflection but with a smoother seamless bend compared to that of a conventional hinge. The position of the wire in Fig. 3 is an initially suggested position. It should be noted that the finalized 3-D model that will be studied is the one shown in Fig. 4, where the wire will be inserted during the structural analysis and presented as beam elements, spars and actuators were not included in the structural analysis, Fig. 3 is provided for illustration purposes.

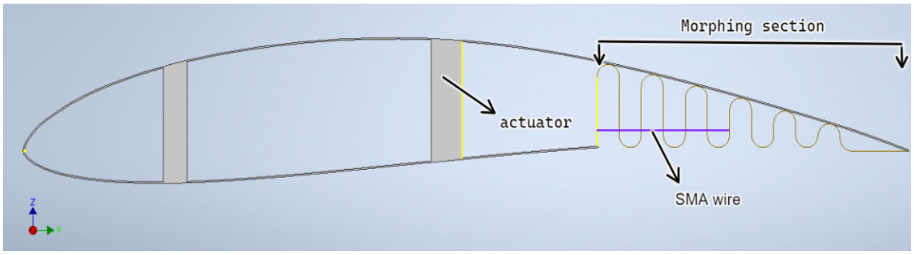

**Fig. 3** The proposed morphing methodology studied in this paper

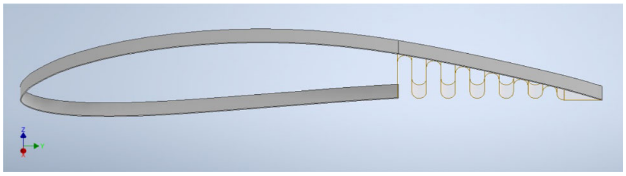

**Fig. 4** Finalized 3D model of the proposed morphing airfoil

**Table 2** Ti-50.8 at%Ni–NiTi wire material properties [22–24]

| Property | Value |
|---|---|
| Austenite elastic modulus (MPa) | 51,700 |
| Martensite elastic modulus (MPa) | 46,000 |
| Poisson's ratio | 0.3 |
| Hardening parameter, $H$, (MPa) | 145 |
| Elastic limit, $R$, (MPa) | 167 |
| Temperature scaling parameter $\beta$ (MPa $\mathrm{C}^{\circ -1}$) | 5.6 |
| Maximum strain (mm/mm) | 0.04 |
| Density (kgm$^{-3}$) | 6450 |
| Martensite finish temperature, $M_\mathrm{s}$ (°C) | − 65 |
| Martensite start temperature, $M_\mathrm{f}$ (°C) | − 95 |
| Austenite finish temperature, $A_\mathrm{s}$ (°C) | − 55 |
| Austenite start temperature, $A_\mathrm{f}$ (°C) | − 15 |
| Reference temperature (°C) | − 100 |

### 2.2.2 Numerical Model of the SMA Wire

Before integrating the shape memory alloy wire into the designed airfoil model, its behavior is simply studied using a commercial finite element method (FEM) software (ANSYS Mechanical 2022 R2) to understand the expected behavior. The chosen material properties that were used as a material input in the analysis is for a NiTi (Ti-50.8 at %Ni) wire which was taken from [22–24] and presented in Table 2. ANSYS software, has a built-in constitutive model which is based on the equations of Aurrichio and Petrini [18, 19] that can simulate the behaviors of shape memory effect and superelasticity, given the right conditions and valid material properties and which was also studied and verified by [20–22].

The wire like structure was presented by a solid cylindrical geometry of 100 mm in length and 1 mm in radius and modelled by 20-node 3-D quadratic solid elements seen in Fig. 5. One of the cylinder ends was held fixed by a fixed support. Since the chosen material can handle maximum recoverable strain of 4%, a displacement condition was applied to the other end of the wire of about 4 mm. The analysis uses a sparse direct solver paired with a Newton–Raphson option and starts with loading the wire with a 4 mm displacement and held for 1 s then it is unloaded. Two main simulations were done to understand the behavior at two loading temperatures the first one had a thermal condition set at reference temperature of about $T = 173.15$ K which is also less than the martensitic finishing temperature and defined as (S1) and the second one had the thermal condition set to a temperature $T = 265$ K, which is higher than that of austenitic finish temperature, at loading and unloading, defined by (S2). To accomplish an accurate and suitable mesh size and also to reduce computational memory and time required to run the simulation, grid refinement tests were conducted on various mesh sizes and total number of elements ranging from about 2000 elements to about 11,000 elements. It was noted that convergence was reached after 8000 elements as seen in Fig. 5.

## 2.3 Numerical Analysis of the Proposed Morphing Design

After simulating the shape memory alloy wire and understanding how it reacts, the structural analysis to test the structural integrity and validity of the proposed design was also studied by using the commercial finite element method (FEM) software (ANSYS Mechanical 2022 R2). The structural analysis is considered a very critical step in which it will provide information about the structure's flexibility and investigate the feasibility of the proposed morphing design as well as the amount of deflection the SMA wire can achieve as well as the effect of the position of the wire on the obtained results. To begin the simulation first the 3D-model presented in Fig. 4 was converted to CATIAv5 [31] to be imported into ANSYS. To integrate the wire into the 3D model, the model was adjusted in SpaceClaim design modeler [32] where the wire was modelled by a circular cross-sectional beam with a radius of 1 mm. The wire was inserted through the corrugated structure near the lower surface of the airfoil at an

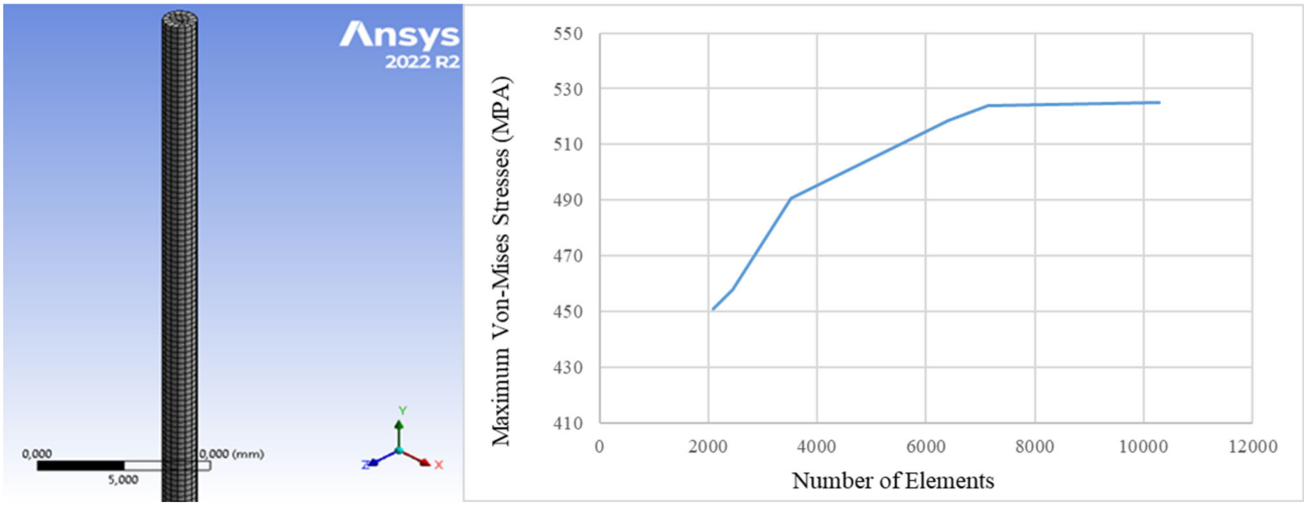

**Fig. 5** Numerical model and mesh refinement of the SMA wire

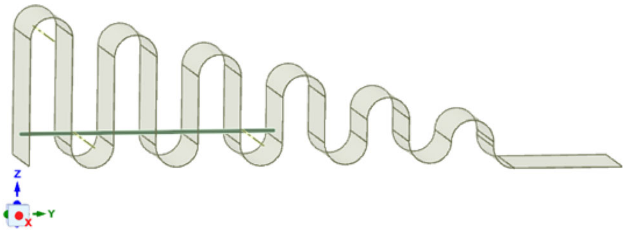

**Fig. 6** Wire insertion position

initially selected position of 20 mm with respect to the vertical $Z$-axis and a length of 150 mm as shown in Fig. 6. The length of the SMA wire depended on its position. A short wire configuration was initially chosen to cover only half of the corrugated structure which was assumed to be sufficient to act like the conventional flap and provide the required downward deflection as shown in Fig. 6. Large deformations and contacts between the wire and the corrugated structure are taken into account while estimating the morphing section's deformation and the wire's pulling action.

The airfoil structure was modeled by three-dimensional 10-Node structural solid elements, three-dimensional 4-node structural shell for the corrugated structure, and 2-Node structural beam elements for the wire. The material chosen for the corrugated structure and the airfoil structure was carbon fiber (CF) with material properties listed in Table 3, the wire had the same material properties of nickel titanium as mentioned as listed in Table 1. Since the trailing edge is only the part considered that will be morphing, the rest of the airfoil starting from 0% chord till 65% chord with respect to the leading edge was held fixed, hence fixed boundary condition was selected as indicated by A in Fig. 7a. Next, corrugated structures were namely bonded to the upper surface of the airfoil at contact points as seen in Fig. 7b, hence creating a unified structure that can move and deform together. Indicated as C in Fig. 7a, one end of the wire beam was tied to the corrugated structure making the wire constrained in the airfoil thickness direction but allowed to move in the wire axis direction except the end of the wire. Indicated as B, the other end of the wire namely its vertex was exposed to a displacement in the opposite $Y$-direction according to the shown axis in Fig. 7a. It should be noted that friction effects were neglected between the shell elements and the wire elements for simplicity, additionally aerodynamic forces were not considered in the structural analysis.

**Table 3** Material properties for carbon fiber

| Property | Values |
|---|---|
| Density (kg $m^{-3}$) | 1800 |
| Poisson ratio $XY$ | 0.2 |
| Poisson ratio $XZ$ | 0.4 |
| Poisson ratio $YZ$ | 0.2 |
| Tensile strength (GPa) | 2.5 |
| Young's modulus $X$ (GPa) | 395 |
| Young's modulus $Y$ (MPa) | 6000 |
| Young's modulus $Z$ (MPa) | 6000 |
| Shear modulus $XY$ (MPa) | 8000 |
| Shear modulus $XZ$ (MPa) | 8000 |
| Shear modulus $YZ$ (MPa) | 2142.9 |

The boundary conditions applied to the wire beam was the same as that of Sect. 2.2 except the displacement was set to 6 mm equivalent to a 4% percent strain of the SMA wire's length which was set as 150 mm. One cycle of pseudoelasticity was conducted. The actuation process consists of displacing the wire 6 mm in the opposite $Y$-direction, with respect to the shown axis, holding it for 1 s at thermal condition above the austenite finishing temperature of $T = 265$ K. The first vertical plate, at which the morphing section begins

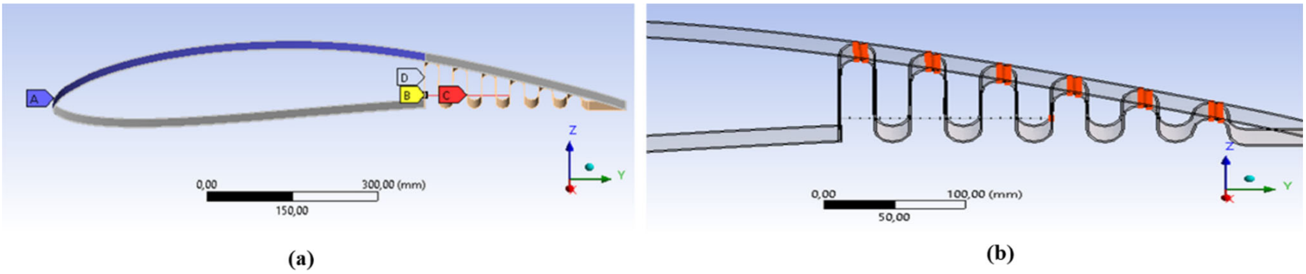

(a)

(b)

**Fig. 7** **a** Boundary conditions applied, **b** bonded corrugated structures to the upper surface

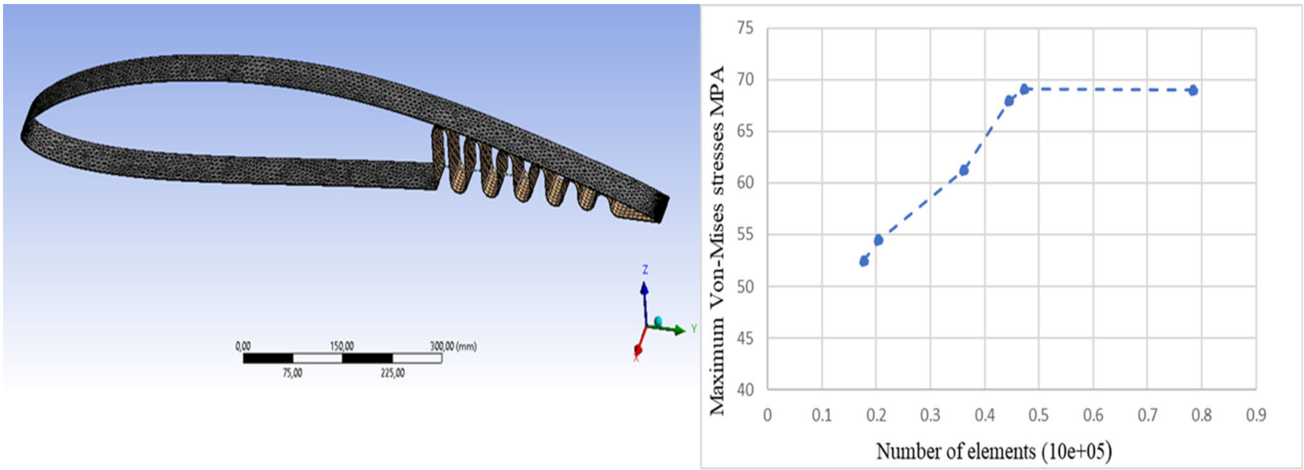

**Fig. 8** Meshed 3D model of the morphing airfoil and mesh refinement analysis

and where the beginning of the wire is placed and subjected to the pulling movement, was also held fixed to avoid any separation of the corrugated structure or structural yielding. Similarly, to achieve an accurate and suitable mesh size and also to reduce computational memory and time required to run the simulation, grid refinement tests were conducted on various mesh sizes and total number of elements ranging from 45,000 elements till about 80,000 elements. To reduce computational time and memory, the finalized properties of the chosen mesh were 49,722 elements with contact elements included and 78,378 nodes as seen in Fig. 8.

## 2.4 Preliminary Results

Obtaining results from the wire study can be presented in Fig. 9, which shows once cycle of super-elasticity presented when the wire is loaded and unloaded at a temperature higher than the finishing austenite temperature, which is the typically expected behavior required to demonstrate pseudo-elasticity. The other simulation conducted at the reference temperature is only for comparison purposes to understand how the super elastic behavior since it requires the working temperature to be above the austenite finishing temperature. S1 which is the simulation conducted at reference temperature, demonstrates that the wire does not return to its pre-strained condition S2 demonstrates the return of the wire to its pre-strained condition after unloading. After the wire simulation was conducted to understand its mechanism, structural analysis of the proposed morphing airfoil was then conducted.

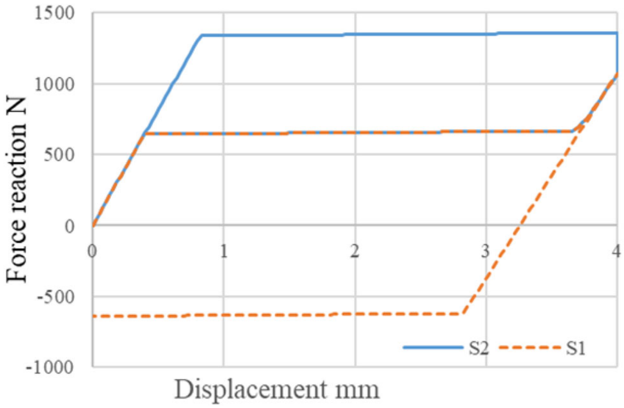

**Fig. 9** Wire study results for behavioral check (S1 at $T = 173.15$ K, S2 at $T = 265$ K)

The structural analysis considered the boundary conditions mentioned in Sect. 2.3. The main aim of developing a numerical model from the proposed morphing concept is to study the feasibility of the use of shape memory allow wires as an actuating mechanism while using corrugated structures as an additional structural support tool that can aid in morphing deflections as well. The first analysis uses a shape

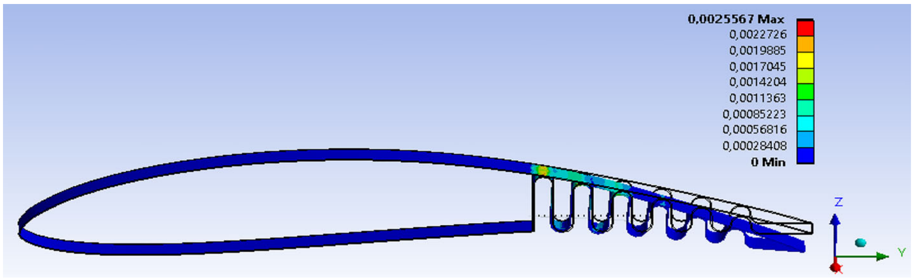

**Fig. 10** Schematic view of the resulting deflection and strain distribution

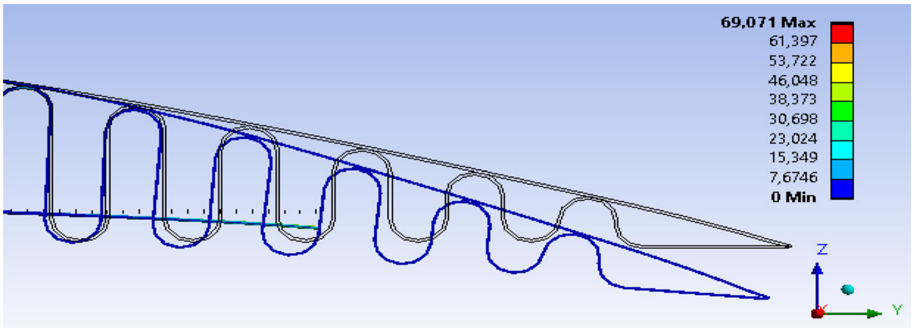

**Fig. 11** Close-up of the amount of downward deflection

memory alloy wire at low position of 20 mm with respect to the *Z*-axis and at exactly in the center of the airfoil of width 50 mm making it positioned at 0 mm with respect to the *X*-axis as displayed in Fig. 6.The results obtained from the initially proposed wire position placement which was at 20 mm with respect to the *Z*-axis, were as follows: (1) The morphing section of the airfoil was able to deflect downwards as similar to the downward deflection of the that of a flap. (2) The resulting geometry showcased a smooth seamless curved bending of the airfoil structure with no structural separation or wire separation as illustrated in Fig. 10. (3) The amount of downward vertical displacement of the airfoil that the wire was able to achieve in the first studied wire position was found out to be 29.008 mm in the *Z* direction as seen in Fig. 11. The $\beta$ angle, which is equivalent to the amount of rotation the morphing section travelled downwards deflection angle, is obtained as 5.69°. The maximum effective stress occurred at the upper surface of the morphing section at position between 65% chord to about 69% chord and this is due to the fact that the beginning of the morphing section starts its downward bending from 65% chord position creating a smooth curved bend unlike that of the hinged control surface. The maximum stress yielded with a value of 69.071 MPa was within the allowed range of (CF) which ensured no structural yielding of the material during actuation. The maximum elastic strain reached by the morphing airfoil when fully deflected was 2.55e−03 mm/mm. From the initial results obtained; the proposed methodology deemed feasible.

## 2.5 Parametric Study

A parametric study was conducted on several different configurations where the main objective of simulating and testing several airfoils with different configurations of positions and numbers of SMA wires is to compare and determine the most suitable configurations of SMA location so that the actuation of the airfoil produces a sufficiently large trailing edge deflection while still having a smooth surface deformation. The cases studied can be summarized in Table 4 where different positions and number of wires were tested to evaluate which configuration can yield a greater deflection angle and to study the relation between the tip deflection and the wire position.

### 2.5.1 Parametric Study Results

After running the simulations and studying about nine different wire configurations, it is found out that the amount of deflection seemed to increase with respect to its vertical position with respect to the Z-axis, as the wire approaches the upper surface of the airfoil the greater the deflection. As seen from Table 5, S6 wire configuration caused very high stress to the structure and also demonstrated structural failure near the beginning of the morphing section where the skin between two consecutive corrugated loops caused lateral buckling as seen in Fig. 12. Additionally in Fig. 13, Fig. 14, it is noted that placing two or three wires adjacent to each other as in the cases of M1 and M2 did not have a significant effect on the amount of deflection but rather caused increased values

**Table 4** Case studies of different wire configurations

| Wire configuration | Description | Conditions |
|---|---|---|
| S6 | Six small wires positioned each in one of the upper corrugated structures with length of 25 mm each | 1 mm displacement which accounts for 4% strain was applied to one end of each wire while the other end was held fixed to the corrugated structure |
| M1 | Two wires placed 25 mm apart adjacent to each other at the same elevation of 20 mm with respect to the *Z*-axis | Same length and loading conditions as mention in Sect. 2.3 |
| M2 | Three wires placed 12.5 mm apart adjacent to each other at the same elevation of 20 mm with respect to the *Z*-axis | Same length and loading conditions as mention in Sect. 2.3 |
| M3 | Two wires placed on top of each other with 5 mm spacings, positioned at 20 mm and 25 mm respectively with respect to the *Z*-axis | Same length and loading conditions as mention in Sect. 2.3 |
| M4 | Two wires placed on top of each other with 10 mm spacings, positioned at 20 mm and 30 mm respectively with respect to the *Z*-axis | Same length and loading conditions as mention in Sect. 2.3 |
| P1, P2, P3, P4, P5 | One wire positioned at different elevations with respect to the *Z*-axis of 20, 25, 30, 35, and 40 mm where they represent P1, P2, P3, P4, P5 respectively | Same length and loading conditions as mention in Sect. 2.3 |

**Table 5** Result summary of wire configuration case studies

| Wire configuration | Stress results MPa | Strain results $\times 10^{-3}$ mm/mm | Tip deflection mm | Result |
|---|---|---|---|---|
| S6 | 633.13 | 9.99 | 7.66 | Structural failure |
| M1 | 70.53 | 2.62 | 29.031 | $\beta = 5.6°$ |
| M2 | 71.89 | 2.68 | 29.045 | $\beta = 5.6°$ |
| M3 | 168.46 | 2.78 | 31.39 | $\beta = 6.07°$ |
| M4 | 260.42 | 3.13 | 34.34 | $\beta = 6.63°$ |
| P1 | 69.071 | 2.55 | 29.008 | $\beta = 5.69°$ |
| P2 | 76.06 | 2.85 | 31.54 | $\beta = 6.02°$ |
| P3 | 84.572 | 3.13 | 34.525 | $\beta = 6.66°$ |
| P4 | 95.07 | 3.58 | 38.098 | $\beta = 7.35°$ |
| P5 | 108.33 | 4.01 | 42.42 | $\beta = 8.172°$ |

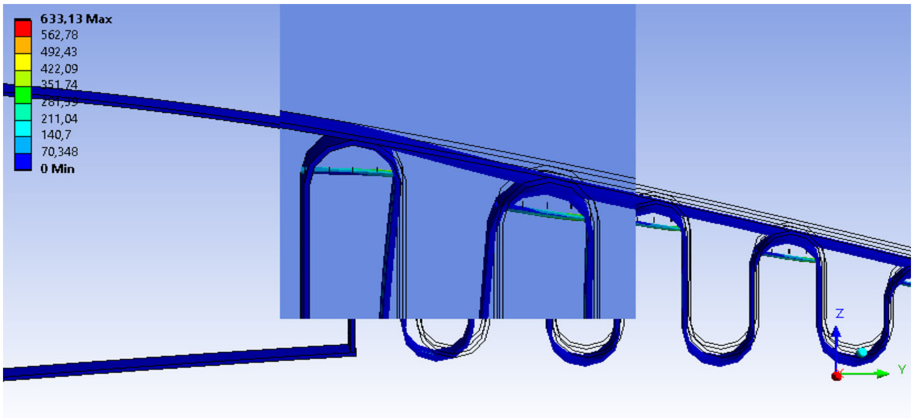

**Fig. 12** S6 wire configuration

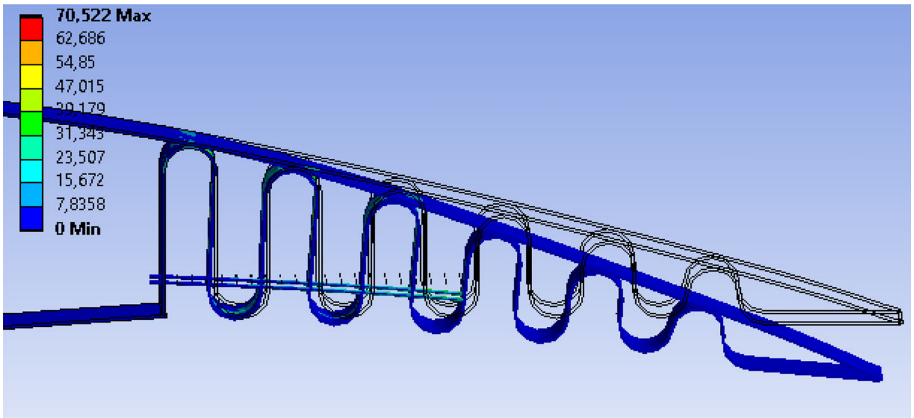

**Fig. 13** M1 wire configuration

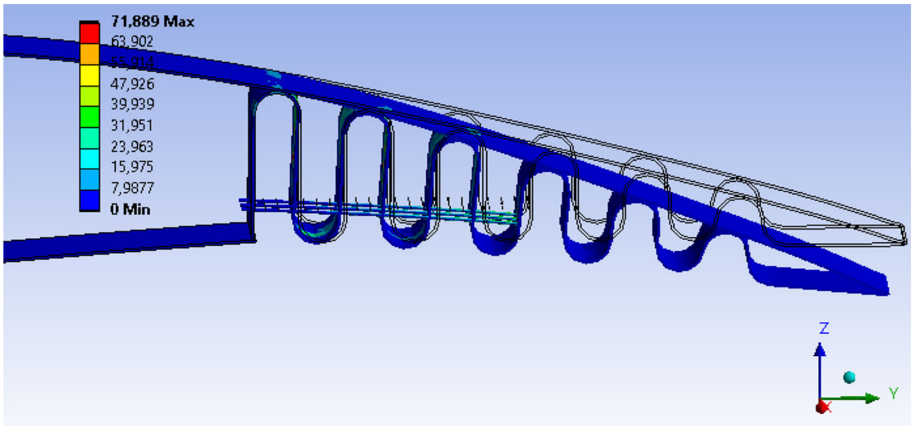

**Fig. 14** M2 wire configuration

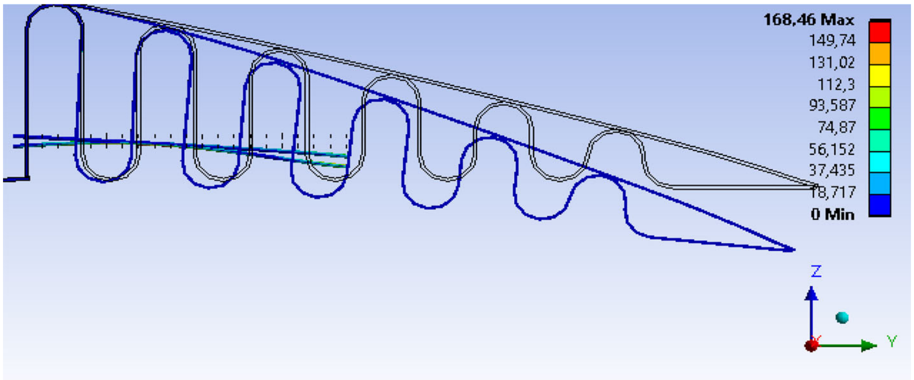

**Fig. 15** M3 wire configuration

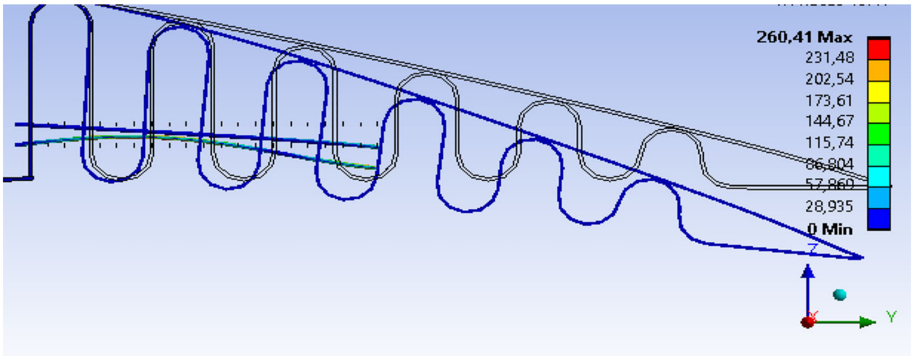

**Fig. 16** M4 wire configuration

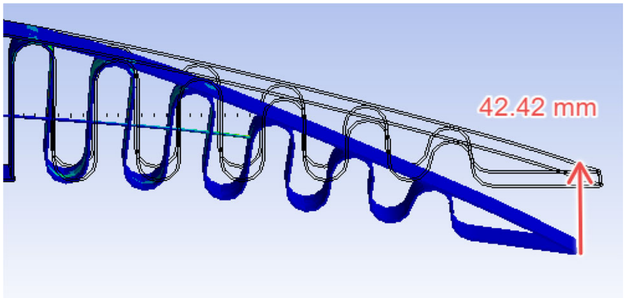

**Fig. 17** P5 wire configuration

of structural stress if it's compared to the initial wire configuration which was studied in Sect. 2.4. Moreover in Fig. 15, Fig. 16, it is noted that placing two wires above one another with either 5 mm or 10 mm spacing as in the cases of M3 and M4, resulted in a slight increase in the amount of tip deflection. In fact, it was noticed that it is obtained mainly from the wire placed at a higher elevation.

In addition, the wires seemed to deform on top of each other which caused added stress to the structure, which can cause additive damage to the corrugated structure with repetitive cycles of flap activation. The results obtained from M3 and M4 provided some information on how the elevation can affect the number of deflections, consequently four more configurations were studied at four different positions with respect to the *Z*-axis as provided in Table 4. Furthermore, the results demonstrated that with increasing elevation the deflection also increased where the largest deflection obtained was at wire configuration P5 and this is because it is very near the upper surface of the airfoil which imitates the effect of the hinge of a conventional flap as seen in Fig. 17.Therefore wire configurations P1, P2, P3, P4, and P5 and their respective deflection angles were used to validate the proposed morphing design by an aerodynamic analysis in Sect. 3.

## 2.6 SMA Wire and Steel Wire Comparison

The aim of this comparative study is to investigate the benefit of using a shape memory alloy and compare the resulting parameters with that of another wire made from a conventional material. Since the obtained angle of deflections from the chosen wire positions P1, P2, P3, P4, and P5 will be studied under aerodynamic conditions, hence the same wire positions were used for a steel wire in order to compare it with the results obtained from P1, P2, P3, P4, and P5. A steel wire with properties labeled in Table 6 was studied under same loading conditions excluding the addition of thermal condition.

**Table 6** Steel properties

| Property | Value |
|---|---|
| Density (kg m$^{-3}$) | 7850 |
| Young's modulus Pa | 2E+11 |
| Poisson's ratio | 0.3 |
| Bulk modulus Pa | 1.66E+11 |
| Shear modulus Pa | 7.69E+11 |
| Tensile yield strength Pa | 2.5E+08 |
| Compressive yield strength Pa | 2.5E+08 |

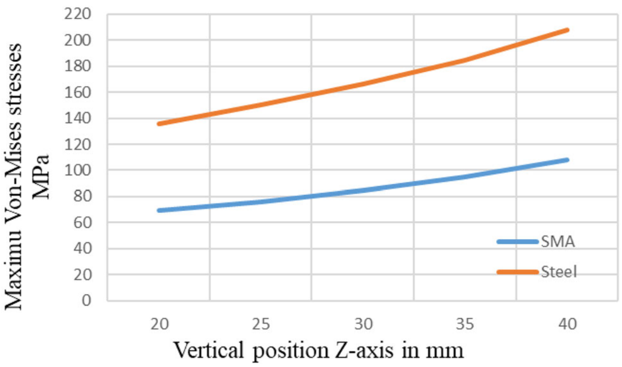

**Fig. 18** Comparison of maximum stress in the airfoil between SMA and Steel wire

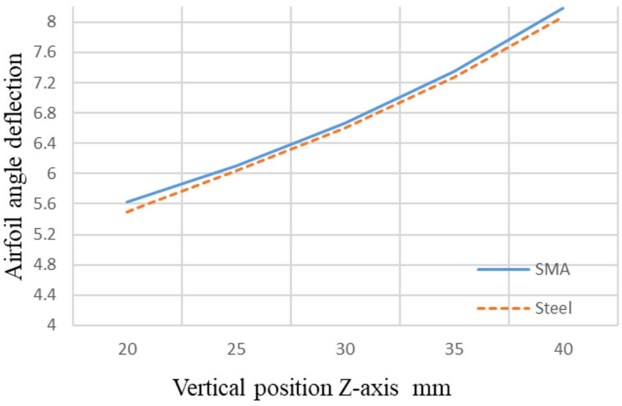

**Fig. 19** Comparison of deflection angles obtained for SMA and steel wires

As seen in Figs. 18 and 19, it can be concluded that the use of shape memory alloy wire has an advantage over its conventional opponent. The obtained maximum stress of the airfoil at maximum downward deflection was almost double for all positions when a steel wire was used, similarly the maximum elastic strain followed also the same trend. In addition, the values of obtained airfoil deflection angle when the SMA wire is implemented are slightly larger than the value obtained when the steel wire is implemented. This is because the SMA wire can handle great amounts of deformation. The obtained results showcased that the use of SMA holds an advantage over the use of a conventional material such as steel. Although the obtained morphing parameters

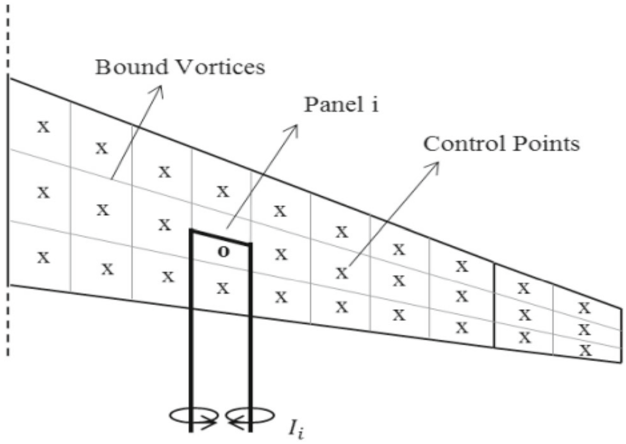

**Fig. 20** Schematic view of panels and bounded vortices [28]

such as deflection angles and vertical downward deflection were somehow similar, the SMA wire has the advantage of being easily manipulated and altered because it can exist at two phases and also has the ability to handle large deformations.

## 3 Aerodynamic Validation of the Proposed Morphing

### 3.1 Methodology

The aerodynamic analysis conducted on the proposed morphing concept of a morphing flap will be compared to its conventional opponent of hinged flap configuration to validate the improvements in aerodynamic performance. The aerodynamic modeling presented uses the panel method integrated in AVL. AVL is a numerical software package which was initially coded in by Younger and further improved by Drela [26]. Modelling is performed by dividing the wing into panels, bound vortices, and control points as seen in Fig. 20. To account for the shape changing geometry parameter which is the trailing edge flap angles, the relevant aerodynamic panel grids are also deflected into the desired angle chosen. One way to showcase the variance in lift is as a step shift between panels. By applying the flow tangency condition, the control points are positioned at 3/4 chord for each panel at the halfway position in the spanwise direction to produce the necessary vortex strength, where the mentioned equation represents the linear sum of the effects of each surface panel's strengths can be created using the Biot–Savart law for each panel

$$\mathrm{d}F = \rho U_{\infty} \times I\mathrm{d}l,$$

where $\mathrm{d}F$ is a force acting on an infinitesimal vortex segment, $\rho$ is air density, $I$ is a displacement vector along an infinitesimal vortex segment, $\mathrm{d}l$ is a displacement vector along an infinitesimal vortex segment and $U_{\infty}$ is the given freestream velocity.

### 3.2 Computational Setup and Numerical Model

To evaluate the obtained enhancements in aerodynamic coefficients which are lift coefficient, drag coefficient, and aerodynamic efficiency, three simulations were conducted where the first one was conducted on un-deflected airfoil model (no flap deployed), the second on the morphing airfoil configuration with a seamless morphing section positioned at 65% chord, and the third on the conventional airfoil with a hinged flap configuration at 75% chord as seen in Fig. 21. It should be noted that the second and the third simulations were conducted at the same deflection angles which were obtained from wire configurations P1, P2, P3, P4, P5, which are $\beta = (5.7°, 6°, 6.7°, 7.4°, 8.2°)$ respectively to account for the change in aerodynamic parameters. It should be noted the angles obtained from the wire configurations were estimated to one decimal place to avoid excessive computational errors during the simulation. The aerodynamic analysis is then conducted over the range of 4 main angle of attacks which namely are ($\alpha = 0°$, $\alpha = 4°$, $\alpha = 8°$, $\alpha = 12°$) with respective free stream velocity of 40m/s and airfoil configuration of 1 m chord and 10-m span [27]. The model used for this study was Maule M-7235B wing model [34]. The flap was defined all over the span of the wing, where the wing planform is equals to 10m$^2$. It should be noted that the studied conventional airfoil and morphing airfoil had five AVL models each, where each model has its own varying angular geometry such as deflection angles of (5.7°, 6°, 6.7°, 7.4°, and8.2°) and studied at four angles of attack.

Next, a grid refinement study was conducted initially at $\alpha = 0°$, to be computationally efficient. Panel grid refinement study was conducted to define the best number of panels to be used to obtain reliable aerodynamic parameters as well as reduce computational cost. Lift and drag coefficients were observed over a several range of panel densities to figure out the sensitivity with respect to the number of panels. As it can be seen from Fig. 21, drag coefficient reached panel insensitivity starting from 1300 panels, however, for lift coefficient it was noted that insensitivity takes place after 1500 panels, hence 1500 panels were considered thereafter to account for both insensitivities. Additionally, all computations thereafter were based on 20 horseshoe vortices along the wing and winglet chord and 75 along the semi-span of the baseline wing and winglet as in Fig. 22.

### 3.3 Results of Aerodynamic Analysis

The conventional hinged flap model has its hinge axis located at 75% chord, and it was evaluated at the corresponding deflections angles which were = (5.7°, 6°, 6.7°, 7.4°, 8.2°).

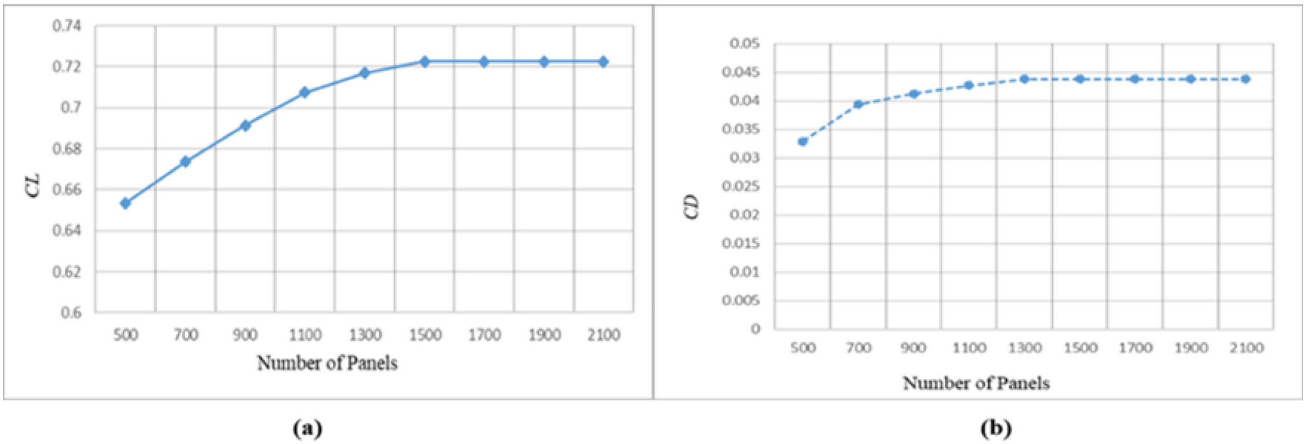

**Fig. 21** Grid refinement analysis for **a** lift coefficient and **b** grid refinement for induced drag coefficients

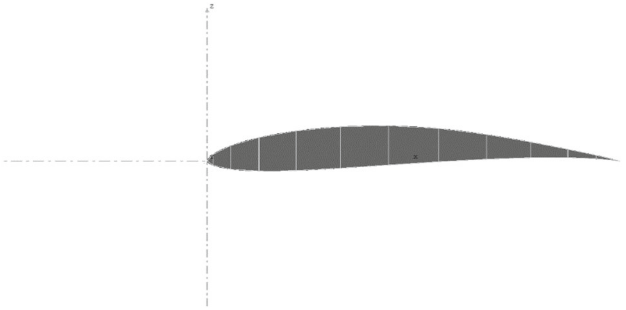

**Fig. 22** Schematic view of undeflected airfoil cross-section

Similarly, the morphing flap model had its flap located at 65% chord corresponding with the beginning of the corrugated structure, and it was evaluated at the same deflection angles. They were both evaluated at the same range of angles of attack ($\alpha = 0°$, $\alpha = 4°$, $\alpha = 8°$, $\alpha = 12°$) and same deflection angles to compare between them as well as investigate the enhancement in aerodynamic coefficients. It should be noted that undeflected flap means that the deflection angle is $\beta = 0°$ and the flap is not activated.

The lift coefficient, drag coefficient, and aerodynamic efficiency which is the ratio between lift coefficient and drag coefficient, were evaluated for the five deflected configurations for the proposed morphing design that were obtained from wire configurations P1, P2, P3, P4, P5. Figure 23 represents the schematic comparison between the undeflected airfoil, airfoil with conventional flap at 75% chord, and morphing airfoil with flap located at 65% chord. The morphing flap has an earlier introduced flap beginning at 65% chord as previously mentioned which is why it will provide a larger surface area that will be deflected, hence is why the morphing airfoil has better geometry as indicated in Fig. 24. Therefore, to clarify, both studied airfoils namely the conventional and morphing flap were both studied at the same range of angles of attack and deflection angles. The aerodynamic study was conducted to compare between the obtained aerodynamic coefficients and to investigate the improvements that will be yielded from the morphing flap.

$$C_L = \frac{L}{\frac{1}{2}\rho V^2 S} \quad C_D = \frac{D}{\frac{1}{2}\rho V^2 S},$$

where $L$ is the lift force, $D$ is the drag force, $\rho$ is the air density, $V$ is the freestream velocity, and $S$ is the wing reference area.

The parameters were then compared to the original aerodynamic coefficients obtained for a conventional hinged plain flap configuration to validate the design from an aerodynamic point of view and provide how the morphing airfoil can obtain better aerodynamic performance. According to the results obtained, it can be noticed that there is an increase in the generated lift coefficient and a decrease in the induced drag coefficient for the morphing flap at all the studied deflection angles $\beta$ when compared to the values of the conventional flap. Additionally, an increase of the aerodynamic efficiency parameter *CL/CD* was noticed at all angles of attack, $\alpha$. To investigate the performance, *CL* coefficient was evaluated for all deflection angles $\beta$. The best enhancements in lift coefficient were obtained mainly at small angles of attack, however, it is still noticed that there were improvements in lift coefficient even at high angles of attack. The maximum percent increase in lift was obtained at $\beta = 5.7°$ and at zero angle of attack. Additionally, it was noted that as the deflection angle increases the percent increase in lift coefficient decreased from 8.65% at $\alpha = 0$ and $\beta = 5.7°$ as seen in Table 7 to almost 6.65% at $\alpha = 0$ and $\beta = 8.2°$ as seen in Table 11.

Similarly, the drag coefficient obtained for the studied deflection angles demonstrated a noticeable drop with a maximum decrement of 2.79% in induced drag obtained at $\alpha = 0$ and $\beta = 5.7°$ which was compared between the conventional flap and morphing flap. The least amount of decrement in induced drag was about 1.17% obtained at $\alpha = 12$ and $\beta =$

**Fig. 23** Trailing edge deflection at $\beta = 5.7°$ comparison between morphing flap, hinged conventional flap, and undeflected airfoil

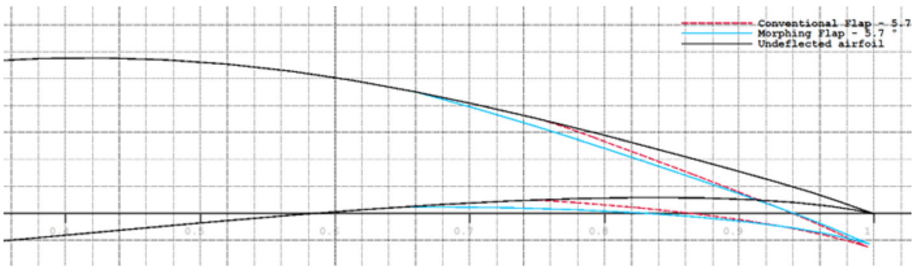

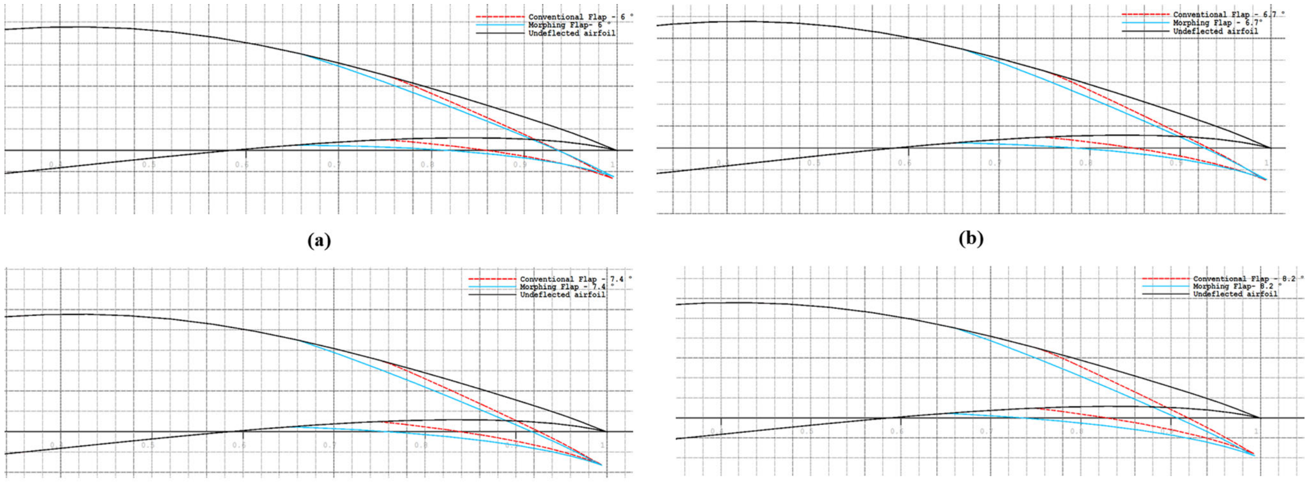

**(a)** **(b)**

**(c)** **(d)**

**Fig. 24** Schematic representations of the aerodynamic analysis conducted on the undeflected flap, morphing flap, and conventional flap at deflection angles **a** $\beta = 6°$, **b** $\beta = 6.7°$, **c** $\beta = 7.4°$, **d** $\beta = 8.2°$

**Table 7** Comparisons percentages between morphing airfoil and conventional airfoil at $\beta = 5.7°$

| $\alpha$, angle of attack (°) | Percent increase in *CL* (%) | Percent decrease in *CD* (%) | Percent increase in aerodynamic efficiency *CL/CD* (%) |
|---|---|---|---|
| 0 | 8.65 | 2.79 | 11.44 |
| 4 | 7.41 | 2.46 | 9.86 |
| 8 | 6.02 | 2.04 | 8.07 |
| 12 | 5.1 | 1.52 | 6.63 |

8.2°, the decrease in drag proves enhanced aerodynamic performance since drag coefficient is considered one of the main factors that affect fuel consumption. Similar to the lift coefficient, the *CD* increment is directly related to the increasing angle of attack as well as increasing flap deployment. The increase in drag resulting from increased deflection angles and angles of attack is seen for both studied flaps, however because of the change in the hinge position and as provided in Tables 7, 8, 9, 10, and 11, the morphing flap had lower values of drag when compared to its conventional opponent at all studied angles $\alpha$ and $\beta$, but the increase in drag that comes with lift is still noticed for all the cases. Therefore,

**Table 8** Comparisons percentages between morphing airfoil and conventional airfoil at $\beta = 6°$

| $\alpha$, angle of attack (°) | Percent increase in *CL* (%) | Percent decrease in *CD* (%) | Percent increase in aerodynamic efficiency *CL/CD* (%) |
|---|---|---|---|
| 0 | 7.79 | 2.46 | 10.25 |
| 4 | 6.84 | 2.19 | 9.03 |
| 8 | 5.65 | 1.82 | 7.47 |
| 12 | 4.85 | 1.37 | 6.22 |

**Table 9** Comparisons percentages between morphing airfoil and conventional airfoil at $\beta = 6.7°$

| $\alpha$, angle of attack (°) | Percent increase in *CL* (%) | Percent decrease in *CD* (%) | Percent increase in aerodynamic efficiency *CL/CD* (%) |
|---|---|---|---|
| 0 | 7.39 | 2.31 | 9.47 |
| 4 | 6.56 | 2.06 | 8.63 |
| 8 | 5.47 | 1.71 | 7.18 |
| 12 | 4.72 | 1.30 | 6.02 |

**Table 10** Comparisons percentages between morphing airfoil and conventional airfoil at $\beta = 7.4°$

| $\alpha$, angle of attack (°) | Percent increase in *CL* (%) | Percent decrease in *CD* (%) | Percent increase in aerodynamic efficiency *CL/CD* (%) |
|---|---|---|---|
| 0 | 7.13 | 2.19 | 9.33 |
| 4 | 6.39 | 1.97 | 8.36 |
| 8 | 5.34 | 1.64 | 6.98 |
| 12 | 4.62 | 1.25 | 5.88 |

**Table 11** Comparisons percentages between morphing airfoil and conventional airfoil at $\beta = 8.2°$

| $\alpha$, angle of attack (°) | Percent increase in *CL* (%) | Percent decrease in *CD* (%) | Percent increase in aerodynamic efficiency *CL/CD* (%) |
|---|---|---|---|
| 0 | 6.65 | 2.0 | 8.65 |
| 4 | 6.05 | 1.81 | 7.86 |
| 8 | 5.11 | 1.51 | 6.61 |
| 12 | 4.45 | 1.17 | 5.62 |

the percent decrement in the drag coefficient in the morphing flap should cause a significant improvement in the aerodynamic performance. Since the results yielded an increase in lift coefficient as well as a decrease in the drag coefficient, the corresponding lift-to-drag ratio showcased an impressive increment especially at low angles of attack such as $\alpha = 0°$ and $\alpha = 4°$. Improvements in aerodynamic efficiency can aid in reduced fuel consumption [25]. Due to increased angle of attack for morphing and conventional flap surfaces, the increment of both lift coefficient and drag coefficient was observed as seen in Tables 7, 8, 9, 10, and 11.

The reason behind the drop in both *CL* percent increment and *CD* percent decrement when comparing flap configurations can be justified and explained as follows. The main purpose of deploying flaps, which are high-lift devices, and creating changes in camber by deflection angles is to increase lift. Additionally, the increase in angle of attack causes an increase in lift coefficient and corresponding induced drag. However, when flaps are deployed in the case of the conventional flap model, the increase in lift is not large because of the geometry consideration of having the flap located at 75% chord when the flap is deflected. In the case of the morphing flap the increase in lift coefficient is slightly larger when compared to the value of the conventional flap since the morphing flap has an earlier introduced flap position at 65% which consequently results in a larger deflected surface area.

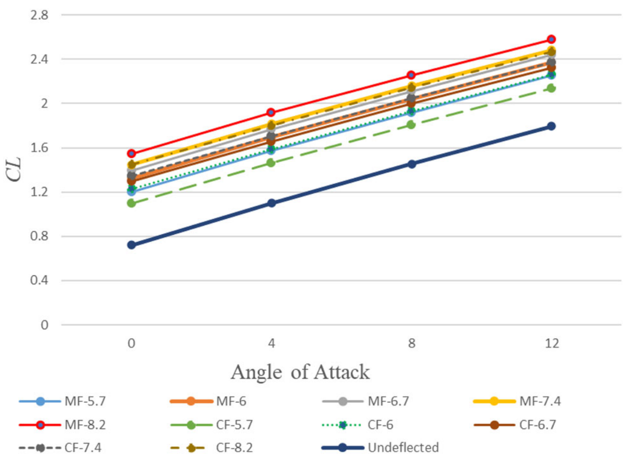

**Fig. 25** Comparison of lift coefficient vs. AoA evaluated at all $\beta = (5.7°, 6°, 6.7°, 7.4°, 8.2°)$ between conventional flap (CF) and morphing flap (MF)

Moreover, the morphing flap has a larger surface area that will be deflected downwards unlike the conventional flap. This is why even at increasing angles of attacks and maximum deflection $\beta$ angle the morphing flap had enhanced aerodynamic parameters. Figures 25, 26, and 27 show the lift coefficient, drag coefficient, and aerodynamic efficiency graphs for the five studied deflection angles $\beta$ for both the morphing and conventional flap. In Fig. 25, the lift coefficient was seen to be improved at all deflection angles as well as angles of attack, but the greatest percent increase was obtained mainly at $\alpha = 0°$ for all $\beta$. Figure 26 showcases that the induced drag was increasing because of increasing $\alpha$, however results deemed that even with large angles of attack the designed morphing airfoil was able to achieve reduced percentages in induced drag for all studied deflection $\beta$ angles. Similarly, in Fig. 27, the results proved enhanced aerodynamic efficiency because of the obtained increase in lift coefficient and decrease in induced drag coefficient. The best noticeable increment of *CL/CD* was obtained at $\beta = 5.7°$ and $\alpha = 0$. The improvement in *CL/CD* for both airfoils between angles of attack $\alpha = 4$ and $\alpha = 8$ for all deflection $\beta$ angles was significantly small which is why Fig. 27 appears to have a constant line between the mentioned angles of attack. Additionally, due to sudden drag CD increase after 8 degrees of attack, the aerodynamic efficiency tends to showcase a plateau in results.

## 4 Conclusion

In this present study, the design methodology associated with morphing flap development was investigated in aims of achieving better aerodynamic performance and to possibly

**Fig. 26** Comparison of induced drag coefficient vs. AoA evaluated at all $\beta = (5.7°, 6°, 6.7°, 7.4°, 8.2°)$ between conventional flap (CF) and morphing flap (MF)

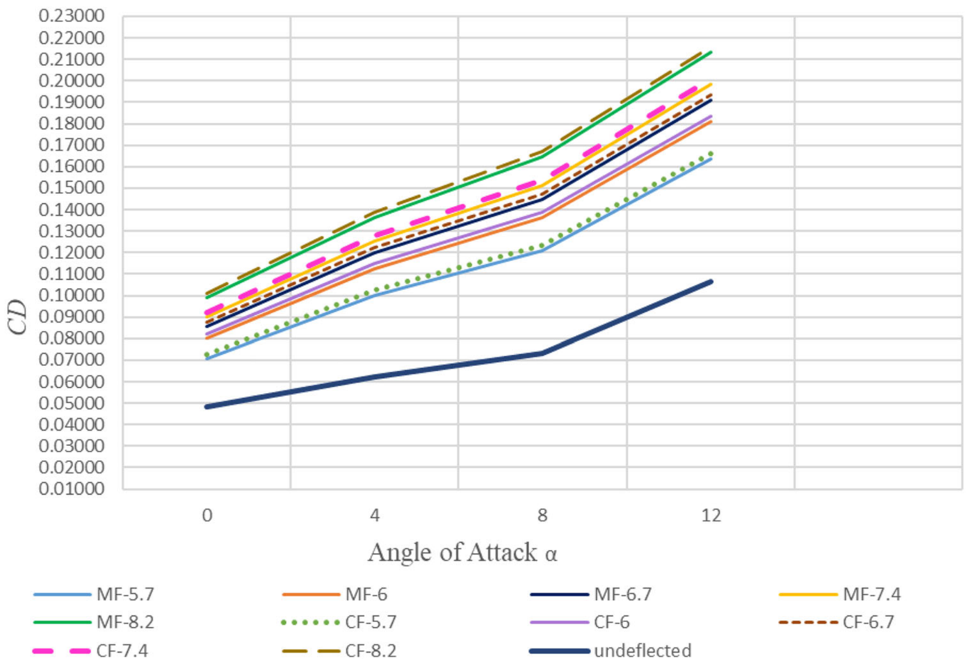

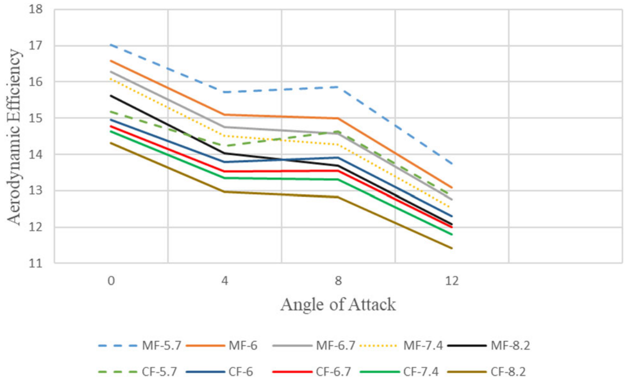

**Fig. 27** Comparison of aerodynamic efficiency vs. AoA evaluated at all $\beta = (5.7°, 6°, 6.7°, 7.4°, 8.2°)$ between conventional flap (CF) and morphing flap (MF)

replace a hinged conventional flap configuration for the studied range of deflection angles $= (5.7°, 6°, 6.7°, 7.4°, 8.2°)$. The proposed design with a smooth deformable morphing flap was studied and compared to its conventional opponent. The design implemented the use of a shape memory alloy wire along with supporting corrugated structures as the actuating mechanism. The proposed design was studied and tested in finite element environment where it proved its feasibility, additionally it was noted that the vertical placement of the wire affected the resulting deflection angle. Although the obtained results seemed to be promising, it should be noted that to deem total feasibility of the design the results obtained in this study needs to be experimentally validated and compared against the computational results. Additionally, the SMA actuation mechanism needs to be studied carefully under the right working temperatures and to be tested in practical application to ensure the validity of the actuation mechanism.

Moreover, the design studied showed that a morphing flap yields better results only for the studied angles, therefore, to implement it for bigger angles another comparison study should be conducted. Next, the aerodynamic performance was evaluated, where it showcased improvements in *CL*, *CD*, and aerodynamic efficiency for the design morphing airfoil compared to its conventional counterpart especially at small angles of attack. The improvement was seen for all deflection angles evaluated at the given range of angle of attacks. The highest achieved increment in lift coefficient, decrement in drag coefficient, and increment in aerodynamic efficiency was obtained at deflection angle $\beta = 5.7°$ and $\alpha = 0°$, when comparing a morphing airfoil to conventional airfoil.

**Acknowledgements** This research did not receive any funding.

**Funding** Open access funding provided by the Scientific and Technological Research Council of Türkiye (TÜBİTAK).

**Data availability** The data that supports the findings in the aerodynamic analysis of this study are available from the author, upon reasonable request.

## Declarations

**Conflict of interest** On behalf of all authors, the corresponding author states that there is no conflict of interest.

## References

1. McRuer D, Graham D (2004) Flight control century: triumphs of the systems approach. J Guid Control Dyn 27(2):161–173
2. Barbarino S, Bilgen O, Ajaj RM, Friswell MI, Inman DJ (2011) A review of morphing aircraft. J Intell Mater Syst Struct 22(9):823–877. https://doi.org/10.1177/1045389X11414084
3. Stanewsky E (2001) Adaptive wing and flow control technology. Progr Aerosp Sci 37(7):583–667. https://doi.org/10.1016/S0376-0421(01)00017-3
4. Jha AK, Kudva JN (2004) Morphing aircraft concepts, classifications, and challenges, vol 5388. pp 213–224
5. Neal, Anthony D (2006) Design, development, and analysis of a morphing aircraft model for wind tunnel experimentation. Master thesis, Virginia Polytechnic Institute and State University, Virginia, USA, pp 17–107
6. Kaygan E, Gatto A (2016) Development of an active morphing wing with adaptive skin for enhanced aircraft control and performance. Greener Aviation 2016, October
7. Gatto A, Bourdin P, Friswell MI (2010) Experimental investigation into articulated winglet effects on flying wing surface pressure aerodynamics. J Aircr 47(5):1811–1815. https://doi.org/10.2514/1.C000251
8. Kaygan E (2020) Aerodynamic analysis of morphing winglets for improved commercial aircraft performance. J Aviat 4(1):31–44. https://doi.org/10.30518/jav.716194
9. Otsuka K, Wayman CM (1998) Chapter 1: Introduction. Shape memory materials. Cambridge University Press, Cambridge, pp 1–2
10. Jani JM, Leary M, Subic A, Gibson MA (2014) A review of shape memory alloy research, applications and opportunities. Mater Des 56:1078–1113. https://doi.org/10.1016/j.matdes.2013.11.084
11. Shili L, Wenjie G, Shujun L (2008) Optimal design of compliant trailing edge for shape changing. Chin J Aeronaut 21(2):187–192. https://doi.org/10.1016/S1000-9361(08)60024-2
12. Campanile LF, Sachau D (2000) The belt-rib concept: a structronic approach to variable camber. J Intell Mater Syst Struct 11(3):215–224. https://doi.org/10.1106/6H4B-HBW3-VDJ8-NB8A
13. de Almeida TC, De Sousa Santos O, Otubo J (2015) Construction of a morphing wing rib actuated by a NiTi wire. J Aerosp Technol Manag 7(4):454–464
14. Ko S, Bae J-S, Rho J-H (2014) Development of a morphing flap using shape memory alloy actuators: the aerodynamic characteristics of a morphing flap. Smart Mater Struct 23:074015. https://doi.org/10.1088/0964-1726/23/7/074015
15. Woods BK, Bilgen O, Friswell MI (2014) Wind tunnel testing of the fish bone active camber morphing concept. J Intell Mater Syst Struct 25(7):772–785
16. Takahashi H, Yokozeki T, Hirano Y (2016) Development of variable camber wing with morphing leading and trailing sections using corrugated structures. J Intell Mater Syst Struct 27(20):2827–2836
17. Kumar TRS, Venugopal S, Ramakrishna Nanda B, Vijay S (2020) Aerodynamic performance estimation of camber morphing airfoils for small unmanned aerial vehicle. J Aerosp Tecnol Manag 12:e1420. https://doi.org/10.5028/jatm.v12.1094
18. Auricchio F, Petrini L (2002) Improvements and algorithmical considerations on a recent three-dimensional model describing stress induced solid phase transformations. Int J Numer Methods Eng 55(11):1255–1284
19. Auricchio F (2001) Robust integration-algorithm for a finite-strain shape-memory-alloy. Int J Plastic 17(7):971–990
20. El Mtili C, Khamlichi A, Hessissen L, Waqas Badar HM (2022) Force-displacement relationships for NiTi alloy helical springs by using ANSYS: Superelasticity and shape memory effect. Int Rev Appl Sci Eng 13(3):309–320. https://doi.org/10.1556/1848.2021.00389
21. Sobrinho JMB, Filho FMF, Emiliava A, Cunha MF, Souto CR, Silva SA, Ries A (2020) Experimental and numerical analyses of a rotary motor using shape memory alloy mini springs. Sens Actuators A Phys 302(1):111823
22. Alazzawi S, Filip P (2019) Modeling the transient behavior of the NiTi shape memory actuator using finite element analysis: parametric study of the rate effects. Results Mater 1:100015. https://doi.org/10.1016/j.rinma.2019.100015
23. Gumpel P, Fuentes JMG, Joachim S (2002) Phase change behaviour of Nitinol shape memory alloys: influence of heat and thermomechanical treatments. Adv Eng Mater 4(7):437–452
24. Filip P, Mazanec K (1994) Influence of work hardening on the reactive stress in a TiNi shape memory alloy. Mater Sci Eng, A 174(2):L41–L43
25. Anderson JD (1991) Chapter 4: Incompressible flow over airfoils. Fundamentals of aerodynamics. McGraw-Hill, New York, pp 247–314
26. Drela M, Youngren H. Project 4—aircraft aerodynamic characteristics. pp 1–7
27. AeroExpo (n.d.) M-7-235B—4-seater private plane by Maule Air, Inc.: AeroExpo. The B2B marketplace for aeronautical equipment. https://www.aeroexpo.online/prod/maule-air-inc/product-180400-36648.html. Accessed 20 Nov 2023
28. Kaygan E, Ulusoy C (2018) Effectiveness of twist morphing wing on aerodynamic performance and control of an aircraft. J Aviat 2:77–86
29. Airfoiltools.com/airfoil/details?Airfoil=e397-il. Accessed 10 Nov 2023
30. Barbarino S, Flores EIS, Ajaj RM, Dayyani I, Friswell MI (2014) A review on shape memory alloys with applications to morphing aircraft. Smart Mater Struct 23(6):1–19. https://doi.org/10.1088/0964-1726/23/6/063001
31. Catia (2023) Dassault Systèmes. https://www.3ds.com/products-services/catia/
32. Ansys SpaceClaim | 3D CAD modeling software. Ansys. (n.d.-a) https://www.ansys.com/products/3d-design/ansys-spaceclaim
33. HavKar (2018) Main components in the aircraft structure and describe their function - wings. HavKar. https://havkar.com/en/blog/view/main-components-in-the-aircraft-structure-and-describe-their-function-wings/80
34. Taylor MJH (1989) Jane's encyclopedia of aviation. Studio Editions, London